Elevated Temperature Solid Particle Erosion Performance of Plasma-Sprayed Co-based Composite Coatings with Additions of Al$_2$O$_3$ and CeO$_2$

H.S. Nithin, Vijay Desai, and M.R. Ramesh

In this paper, investigation into solid particle erosion behavior of atmospheric plasma-sprayed composite coating of CoCrAlY reinforced with Al$_2$O$_3$ and CeO$_2$ oxides on Superni 76 at elevated temperature of 600 °C is presented. Alumina particles are used as erodent at two impact angles of 30° and 90°. The microstructure, porosity, hardness, toughness and adhesion properties of the as-sprayed coatings are studied. The effects of temperature and phase transformation in the coatings during erosion process are analyzed using XRD and EDS techniques. Optical profilometer is used for accurate elucidation of erosion volume loss. CoCrAlY/CeO$_2$ coating showed better erosion resistance with a volume loss of about 50% of what was observed in case of CoCrAlY/Al$_2$O$_3$/YSZ coating. Lower erosion loss is observed at 90° as compared to 30° impact angle. The erosion mechanism evaluated using SEM micrograph revealed that the coatings experienced ductile fracture exhibiting severe deformation with unusual oxide cracks. Reinforced metal oxides provide shielding effect for erodent impact, enabling better erosion resistance. The oxidation of the coating due to high-temperature exposure reforms erosion process into oxidation-modified erosion process.

1. Introduction

Among the major objectives of improving surface characteristics of the materials for better performance, resistance to erosion has been one of the top priorities of material researchers. One of the major concerns of material degradation in tribological issues is solid particle erosion (SPE), which is defined as the loss of material caused by impact of hard solid particles on the target material (Ref 1). This phenomenon is severe under higher temperature and velocity of impinging particles. There are several components of gas turbine, which are subjected to solid particle erosion at the intermediate temperature ranges between 500 and 600 °C, such as compressor outlet blades, vanes and disks, turbine exit blades, vanes and disks and turbine inlet disks and outer casing (Ref 2, 3). Sand particles and volcanic ashes are the principal erosion sources for aircrafts when they are operating in the vicinity of desert and volcanic areas, where velocities of particles play a major role. Also, SPE is strongly influenced by the size, speed, geometry and on angle of impingement of the erodent particles. The damage to material due to SPE can directly affect the efficiency, operating cost and early failure of the components (Ref 1-4).

The surface engineering of the material for improving resistance to erosion started in 1990s (Ref 1). MCrAlY (M = Ni, Co) overlay coatings are commonly used in high-temperature components to protect the surface against oxidation and hot corrosion (Ref 5). MCrAlY coatings cannot function in multicomponent gaseous environment, where the mechanical properties are deteriorated by combined erosion and corrosion. These coatings experienced severe erosion due to the tendency of softening of material and reduced hardness with the increase in temperature (Ref 5-7).

On the other hand, ceramic coatings deposited on metallic substrates by plasma spraying have considerable attention for wear and corrosion. However, ceramic coatings exhibit porous microstructure and poor inter-splat bonding (Ref 8). The combination of microstructure defects and brittle material property limits the application of ceramic coating. Erosion of plasma-sprayed ceramics coatings is attributed to the failure of the individual splat boundaries (Ref 8-10).

To compensate the reduction of erosion resistance in metallic coatings due to lack of hardness at high temperature and due to porosity in ceramic coatings, combination of metallic ductile phase and ceramic brittle phase has been identified as cost-effective solution. Coatings with multiple phases are preferred in industrial applications to counter degradation due to combined oxidation and wear (Ref 4-16).

Grewal (Ref 3) reported that Ni powder with 40% Al$_2$O$_3$ reinforcement exhibits good erosion resistance than pure Ni with its improved mechanical properties. The effect of the addition of Al$_2$O$_3$ on the mechanical properties of the NiCr cold spray coating was investigated. The hardness was increased up to 45% with the addition of Al$_2$O$_3$ (Ref 14). Kim et al. (Ref 11) suggested that the addition of 20-40 wt.% hard-phase material would improve the mechanical and tribological properties of the coating. The further increment in the hard-phase content can deteriorate the coating properties, due to the increase in

H.S. Nithin, Vijay Desai, and M.R. Ramesh, Department of Mechanical Engineering, National Institute of Technology Karnataka, Surathkal, India. Contact e-mail: nithinshiv1989@gmail.com.

porosity and pore size which is responsible to generate high stress concentration.

The application of rare earth oxides in different coatings was attempted by Wang and Chen (Ref 4) to enhance the properties of the coating in terms of corrosion and wear resistance. The addition of optimum amount of rare earth oxides such as CeO_2, La_2O_3 and Y_2O_3 not only limits corrosion and wear but also enhances the coating properties such as hardness, toughness, bond strength and thermal shock resistance (Ref 4, 8, 13). Wang and Chen (Ref 4) evaluated the mechanical and erosion properties of NiAl coating with 2, 5 and 8 weight percentage of CeO_2. He suggested that 2% CeO_2 in NiAl matrix provides better mechanical and erosion properties.

Although several researchers have investigated the benefits of composites coatings, most of them are the combination of pure metal/intermetallic with brittle oxides (Ref 3, 4, 7, 11-14). However, the studies on the combination of unique MCrAlY alloy and oxide reinforcement are still very limited (Ref 17, 18).

In the present work, erosion performance of plasma-sprayed $CoCrAlY/Al_2O_3/YSZ$ and $CoCrAlY/CeO_2$ composite (cermet) coatings is compared. Al_2O_3 and CeO_2 are the materials known for their better properties such as hardness and thermal stability which are essential for extreme working conditions of gas turbine components (Ref 4, 8, 14). The erosion behavior of composite coatings has been studied at elevated temperature of 600 °C at two impingement angles of 30° and 90°. The morphology of eroded surfaces is analyzed to identify the erosion mechanism.

2. Experimental Procedure

2.1 Substrate Material and Coating Characterization

In the present work, nickel-based super alloy—Superni 76—is used as substrate, and the chemical composition is listed in Table 1. The cold-rolled plates of Superni 76 used for making gas turbine blades are procured from M/s MIDANI, Hyderabad. Specimen of 25 mm × 25 mm × 3 mm dimensions was cut from these plates using shearing machine followed by grinding the edges. The specimens are grit blasted using alumina powder of 150 μm size to generate rough pattern on the surface prior to plasma spraying, so as to ensure better adhesion between coating and substrate. The bond coat of NiCrAlY was sprayed on the prepared substrate in order to provide better adhesion of the top coat and also to reduce the thermal expansion mismatch between the top coat and substrate (Ref 19). The chemical composition of CoCrAlY and NiCrAlY powders is mentioned in Table 2. The Co-based composite powder CoCrAlY with the addition of Al_2O_3/YSZ and CeO_2 reinforcements was prepared by planetary ball milling (VB Ceramic, India) with tungsten carbide spherical balls of 10 mm diameter, speed of 300 rpm and the duration of 10 min to ensure proper mixing. The two composite feedstock powders,

namely $CoCrAlY/28\%Al_2O_3/2\%YSZ$ and $CoCrAlY/2\%CeO_2$, were deposited on all the faces of the sample over the bond coat. The reinforcement added to matrix material is in weight percent. The nominal particle size distribution of the coating powders is measured by laser diffraction technique (Cilas 1064, France) as per ASTM C1070 and is reported in Table 3. METCO USA 3 MB plasma spray equipment was used for plasma spray process. The spray parameters adapted during deposition are listed in Table 4.

The metallographic structure of coated samples was examined using JOEL-JSM-6380LA scanning electron microscope (SEM). BIOVIS Materials Plus optical microscope, interfaced with image analyzing software (version 4.58), was used to obtain optical image along the cross section of as-sprayed coatings and to determine the porosity content. Fifteen fields of view were taken per sample at 250× magnification. The microhardness was measured using Omni-tech Vickers tester (MVH-S-AUTO) under 300 g loads and a dwell time of 10 s. The phases in powder and as-sprayed coating were analyzed using x-ray diffractometer (XRD, Rigaku MiniFlex-600).

Table 2 Coating chemical composition (wt.%)

Coating type	Ni	Co	Cr	Al	Y
NiCrAlY	Bal	…	22	9	1
CoCrAlY	…	Bal	23	13	0.5

Table 3 Particles size (μm) distribution of coating powders

Particle size	CoCrAlY/28%Al$_2$O$_3$/2%YSZ	CoCrAlY/2%CeO$_2$
D (0.1)	23.9	16.7
D (0.5)	55.2	45.3
D (0.9)	99.7	91.3
Mean	59.6	51.1

Table 4 Spray parameters of plasma spray process

Argon	
Pressure	0.7 MPa
Flow	40 L/min
Hydrogen	
Pressure	0.35 MPa
Flow	7 L/min
Current	490 A
Voltage	60 V
Powder feed	60 g/min
Stand of distance	100-125 mm

Table 1 Chemical composition (wt.%) of substrate

Substrate	Equivalent	C	Mn	Si	Cr	Mo	Fe	Co	W	Ti	Ni
Superni 76	Hastelloy X	0.08	0.44	0.3	21.87	9.08	20	1.39	0.52	0.14	Bal

2.2 Adhesion Strength and Fracture Toughness Test

Adhesion strength test was carried out using Shimadzu hydraulic tensile testing machine, with a crosshead speed of 0.5 mm/min in accordance with ASTM C633-13 standard. The coated specimens were bonded to a 25-mm-diameter rod using HTK ultra-bond adhesive glue and cured in furnace at 150 °C. Curing enhances the adhesion between coating and glue. The adhesion strength was calculated as ratio of maximum load to the cross-sectional area of sample.

Fracture toughness is one of the significant properties used for evaluating solid particle erosion behavior of the coatings. The toughness is measured by indentation crack technique (Ref 10, 20, 21). The radial crack is produced using a square pyramid indenter along the diagonal of indentation. The fracture toughness is calculated using crack length by the following relations (Ref 10).

$$K_{IC} = 0.0193(H_V d)(E/H_V)^{2/5}(a)^{-1/2} \quad (c/d \leq 2.5)$$
$$\text{Palmqvist Cracks} \quad \text{(Eq 1)}$$

$$K_{IC} = 0.0711\left(H_V d^{1/2}\right)(E/H_V)^{2/5}(c/d)^{-3/2}$$
$$(c/d \geq 2.5) \text{ Half penny Cracks} \quad \text{(Eq 2)}$$

where H_v is the Vickers hardness, E is the Young's modulus, d is the half-diagonal of the Vickers indentation. The radial crack length (a) is equal to the indentation crack length (c) minus the half-diagonal of the Vickers indentation (d). Values of a, c and d were measured using SEM images.

2.3 Erosion Studies

Erosion tests were carried out as per ASTM G76-13 standard using solid particle air jet erosion tester (Ducom-TR-471-800) at temperature of 600 °C in air. Schematic represen-
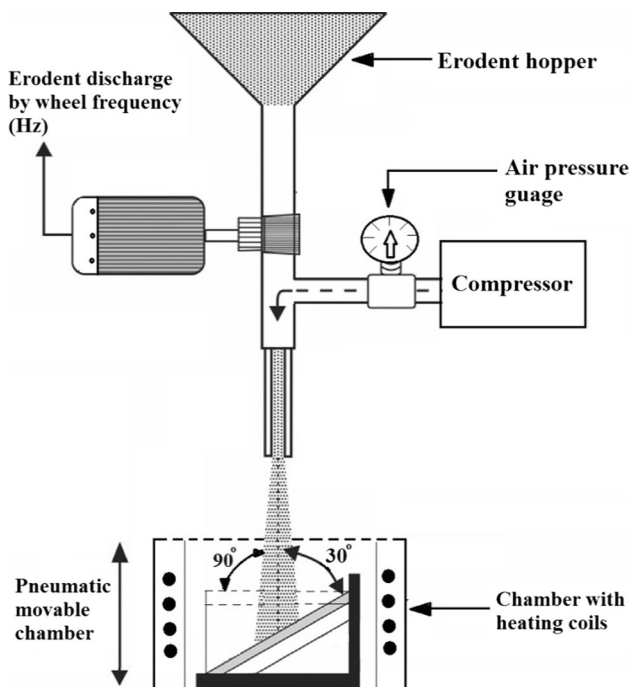
tation of erosion test rig is shown in Fig. 1, and erosion test conditions are presented in Table 4.

Initially, the samples were cleaned using acetone and weighed in electronic weighing balance having least count of 0.001 g to measure bare sample weight. The SPE process was carried out for five cycles with duration of 10 min for each cycle and for each impact angles. After each erosion cycle, the eroded sample was cleaned in acetone using ultrasonicator and dried and weighed to determine the weight loss. This weight loss normalized by the mass of the alumina particles causing the weight loss (i.e., testing time × particle feed rate) was then computed as the dimensionless incremental erosion rate. The above procedure was repeated till the incremental erosion rate attained a constant value independent of the mass of the erodent particles or, equivalently, of testing time. This constant value of the incremental erosion rate was defined as the steady-state erosion rate (Ref 12, 22). Erosion volume loss was also measured using non-contact optical profilometer (Zeta-20). Non-contact optical profiler has the ability to provide three-dimensional profiler patterns with excellent accuracy (Ref 22-24). The scanned surface is profiled by computer-generated map by extracting the data from three-dimensional interferogram of scanned surface. Erosion volume loss is measured by taking difference of volumes obtained before and after erosion.

3. Results and Discussion

3.1 Characterization of As-Sprayed Coatings

The typical microstructure along the cross section of CoCrAlY/Al₂O₃/YSZ and CoCrAlY/CeO₂ coating is shown in Fig. 2(a) and (b). The splats formed by the molten or semi-molten impacting coating particles and their distributions are shown in Fig. 2(c) and (d). The average value of coating thickness was measured from the backscattered electron image, along the coating cross section. The total coating thickness is in the range of 250-300 μm and with bond coat used for better adhesion of top coat, while the top coat thickness is in the range of 150-200 μm. The magnified backscattered image (Fig. 2c, d) manifests densely packed lamellar structure indicating better compacting of molten particles. In case of CoCrAlY/Al₂O₃/YSZ coating, owing to Al₂O₃ (28%), few partially melted particles and pores are observed (Fig. 2c). Al₂O₃ splats are seen as dark gray with the white region showing Co-rich phases. Similarly, CeO₂ particles are distributed along the Co alloy splat boundaries and appear as bright white region. The average porosity of CoCrAlY/Al₂O₃/YSZ and CoCrAlY/CeO₂ coating is measured using image analyzer and is found to be 5.5 and 4%, respectively.

X-ray diffraction pattern of the powder and as-coated samples of CoCrAlY/Al₂O₃/YSZ and CoCrAlY/CeO₂ composites is shown in Fig. 3 and 4, respectively. The major peak in both the powder and as-coated patterns corresponds to Cr and Al₃Co compounds with some metal oxides of Cr₂O₃ and Al₂O₃. Metal oxides are formed due to occurrence of oxidation during in flight time, and it is reported that plasma spray process has longer in flight time compared to other thermal spray process (Ref 7). The reinforcement phases Al₂O₃ and CeO₂ remain unchanged even after the plasma spray process. The dissolution of metal matrix evident the broadening of peak accompanied by reduction in peak intensity at 2θ of about 44°
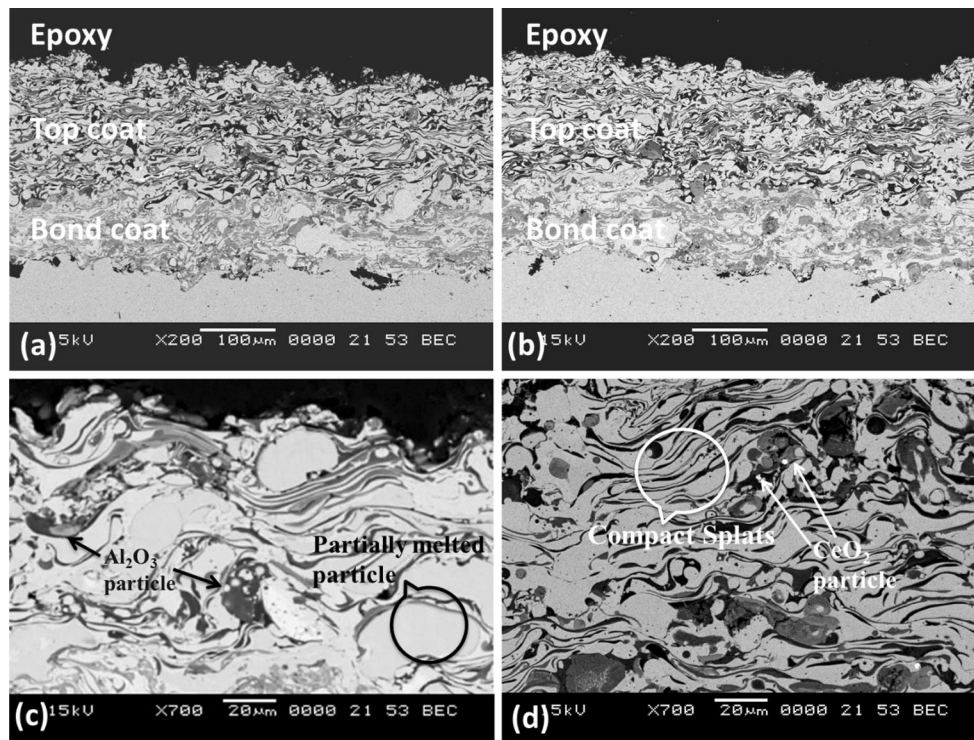

Fig. 1 Schematic of erosion test rig

Fig. 2 SEM micrographs along cross section of CoCrAlY/Al$_2$O$_3$/YSZ (a, c) and CoCrAlY/CeO$_2$ (b, d) coating
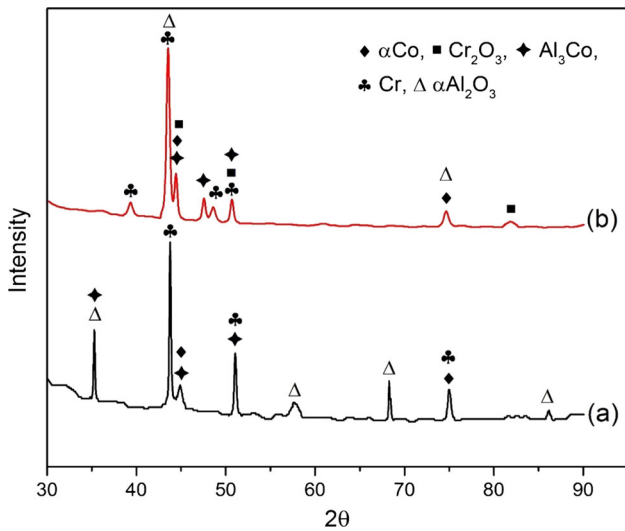

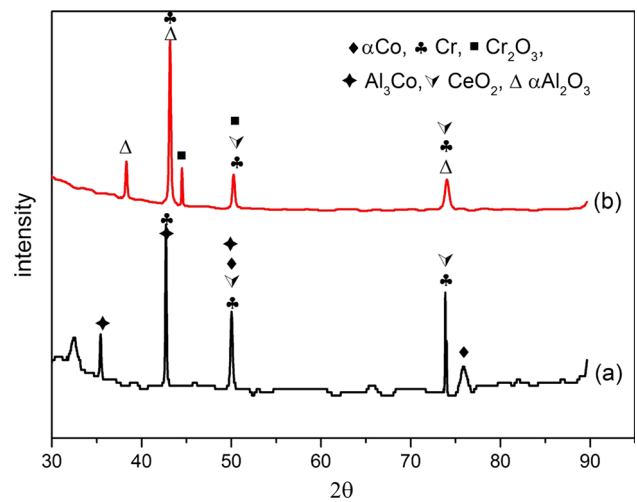**Fig. 3** X-ray diffraction pattern of (a) CoCrAlY/Al$_2$O$_3$/YSZ powder and (b) as-coated

Fig. 4 X-ray diffraction pattern of (a) CoCrAlY/CeO$_2$ powder and (b) as-coated

can be observed for the as-sprayed coating in comparison with the XRD pattern for the initial powder. This difference reveals the formation of slight amorphous matrix. Similar observations are reported by Sundararajan et al. (Ref 25) and Planche et al. (Ref 26).

Figure 5 shows the variation in microhardness values along the substrate and coating. Non-uniformity in microhardness across the cross section of the coatings can be attributed to the microstructural inhomogeneity in the form of hard-phase distribution, porosity, unmelted and partially melted particles in the coating. The distribution of Al$_2$O$_3$ and CeO$_2$ is marked

in Fig. 2(c) and (d), and also these phases are indexed in as-coated XRD pattern (Fig. 3, 4). Average hardness value of CoCrAlY/Al$_2$O$_3$/YSZ and CoCrAlY/CeO$_2$ coatings was measured as 476 and 402 HV, respectively. The hardness of bond coat was found to be 298 HV. It is also observed that the hardness of substrate shows incremental increase in values toward the interface. This is due to strain hardening effect during the grit blasting prior to plasma spray process and due to the compressive stresses developed at the interface because of continuous impact of coating splats during the thermal spray process (Ref 13, 14).

3.2 Adhesion Strength and Fracture Toughness by Indentation

Adhesion strength has good relation with coating thickness; the top coat should be less than 300 μm as per ASTM-C633-13 standard. Better adhesion of the coating is expected for lesser thickness as the effect of internal stress will be lower for smaller thickness. Figure 6 shows the typical fracture occurring between coating and the substrate. The adhesion strengths of CoCrAlY/Al$_2$O$_3$/YSZ and CoCrAlY/CeO$_2$ coatings are found to be 9.24 and 15.65 MPa, respectively. Similar values of

adhesion strength have been reported in coatings containing Al$_2$O$_3$ hard phase such as Cr/Al$_2$O$_3$, ZrO$_2$/Al$_2$O$_3$ and Al$_2$O$_3$ plasma-sprayed coatings (Ref 15, 16, 27).

Morphology of both the coatings showed a clear picture of adhesive failure with fracture occurring between coating and substrate (Ref 27). This shows that the cohesive strength between the splats is better than adhesion strength of coatings. However, the coating adhesion is influenced by microstructural aspects such as unmelted particles, pores, cracks and anisotropic splats formed during spray process. More the unmelted particles in coating have proportional increment with porosity and also decreased coating coherence, which results in reducing the adhesion strength (Ref 28). In this context, CoCrAlY/CeO$_2$ coating exhibited better bond strength and the same can be justified by the compact splats morphology and also distribution of CeO$_2$ particles along the splat boundaries.

The fracture toughness of the coating was measured by indentation crack method considering only those cracks in which crack has propagated along the diagonal of indentation. The crack formed is known as Palmqvist cracks as the ratio of the indentation crack length (c) and the half-diagonal of the Vickers indentation (d) is found to be less than 2.5 in both the coatings (Fig. 7). The average value of fracture toughness (K_{IC}) of CoCrAlY/Al$_2$O$_3$/YSZ and CoCrAlY/CeO$_2$ coatings is found to be 2.8 and 3.6 MPa m$^{1/2}$, respectively. SEM micrographs reveal that cracks mainly propagated in the direction parallel to the coating/substrate interface. The result reveals that coating containing CeO$_2$ reinforcement shows higher toughness as a result of uniform distribution of CeO$_2$ particles along CoCrAlY splats and good cohesion between the splats in the coating. The CoCrAlY/Al$_2$O$_3$/YSZ coating shows long cracks propagated
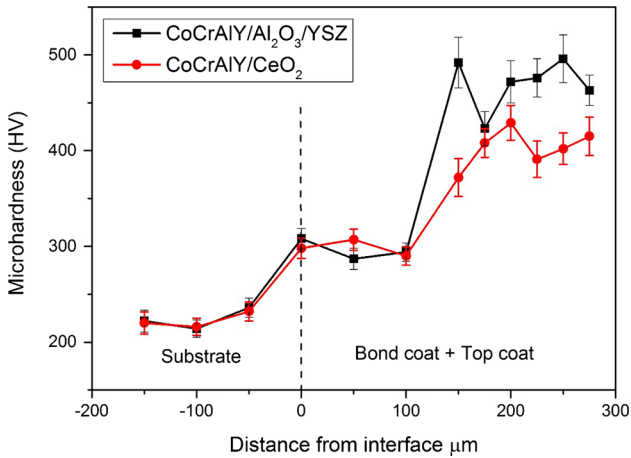

Fig. 5 Microhardness variation along the cross section of CoCrAlY/Al$_2$O$_3$/YSZ and CoCrAlY/CeO$_2$ coating with substrate
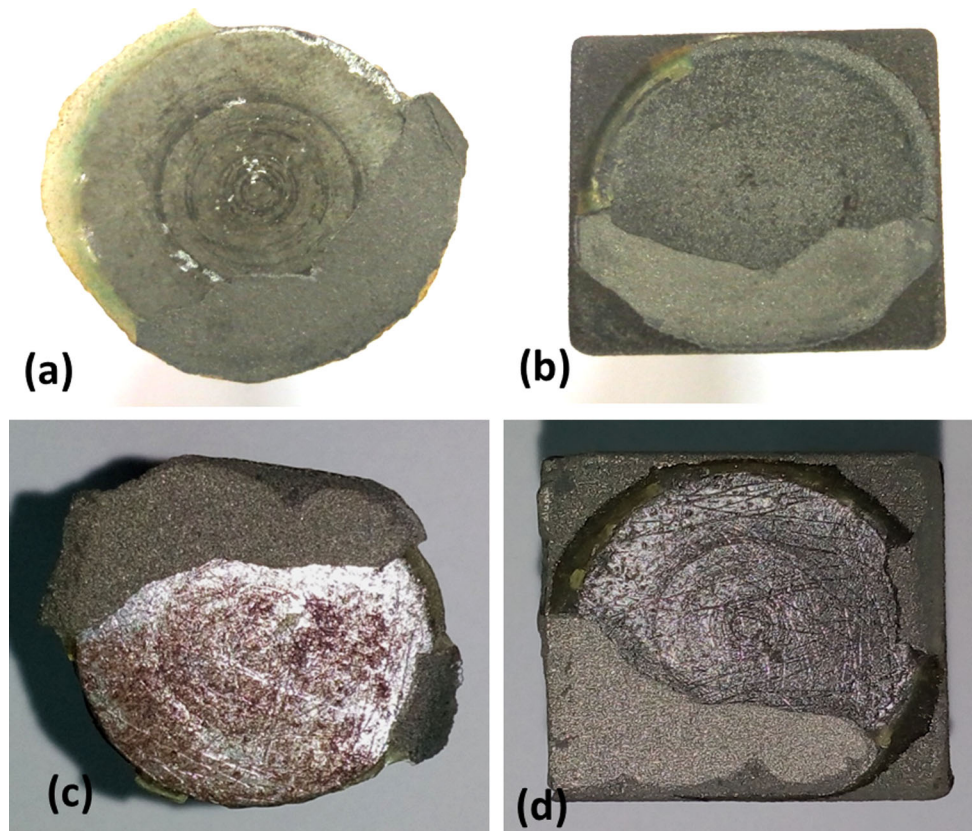

Fig. 6 Fractured surface of adhesion test samples of CoCrAlY/Al$_2$O$_3$/YSZ (a, b) and CoCrAlY/CeO$_2$ (c, d) coating, respectively
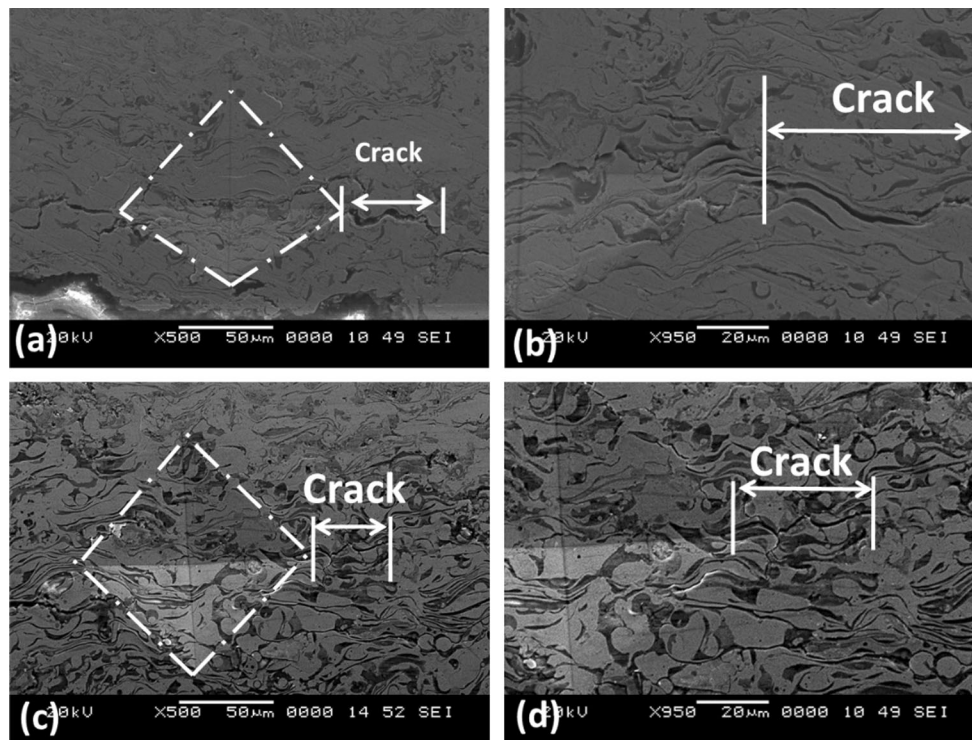
Fig. 7 Micrographs of cracks produced by indentation on (a) CoCrAlY/Al$_2$O$_3$/YSZ and (b) CoCrAlY/CeO$_2$ coating

along the weak inter-splat boundaries with porous structure leading to lower fracture toughness. Also, Al$_2$O$_3$ reinforcement is likely to develop residual stresses during the coating process which cause lower toughness values (Ref 20, 21).

3.3 Oxidation of Coating Surface During Erosion

The XRD pattern of CoCrAlY/Al$_2$O$_3$/YSZ coating (Fig. 8a) subjected to SPE at 600 °C reveals that CoO, α-Al$_2$O$_3$ and AlYO$_3$ as the major phases observed with minor peaks corresponding to Cr$_2$O$_3$. The formation of spinel oxide AlYO$_3$ in coating leads to the fast transformation of metastable alumina to α-Al$_2$O$_3$, which is stable even at high temperature. In case of CoCrAlY/CeO$_2$ coating (Fig. 8b), CoO and α-Al$_2$O$_3$ are major phases with minor peaks corresponding to CeO$_2$ and Cr$_2$O$_3$. It is also observed that major diffraction peak of CoCrAlY/CeO$_2$ coating is wider than that of the CoCrAlY/Al$_2$O$_3$/YSZ coating. It is hypothesized that the grain/splat size of coating decreases with the increase in full-width half-maximum (FWHM) value. The FWHM values of 0.38267 for CoCrAlY/CeO$_2$ and 0.30144 for CoCrAlY/Al$_2$O$_3$/YSZ coating indicate that better splat/grain refinement has occurred in coating containing CeO$_2$. This is due to sub-grain formation or microstructural fragmentation during elevated temperature erosion (Ref 4, 13, 29).

CeO$_2$ being a rare earth oxide acts surface active element which refines the microstructure, resulting in fine splats and better bonding between splats. This microstructural property has a principal influence in restricting the material removal during solid particle erosion (Ref 13).

3.4 Influence of Impact Angle on Solid Particle Erosion

The cumulative erosion loss measured for each cycle of 10 min is shown in Fig. 9. The erosion rate is calculated by dividing the weight loss of coating material by the mass of
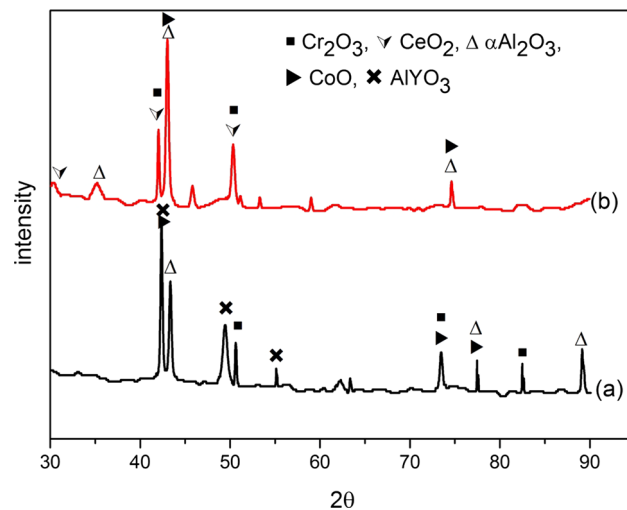

Fig. 8 X-ray diffraction patterns of eroded (a) CoCrAlY/Al$_2$O$_3$/YSZ and (b) CoCrAlY/CeO$_2$ coating at 600 °C

erodent. It is also assumed that all the mass of erodent impacted the target since the erosion scar is within the sample dimension. Superni 76 alloy shows immense variation in the erosion rate in each cycle due to embedding and detaching of alumina erodent. This is due to more ductile nature of substrate at higher temperature. Erosion rate of both the coatings is much lower than Superni 76 alloy as well as lesser variation in erosion rate is observed. Observations of the erosion rate and their variations indicate that, during the initial cycles, the rapid oxidation of active elements of coating leads to formation of protective oxides, resulting in lower erosion rate. The rate at which erosion
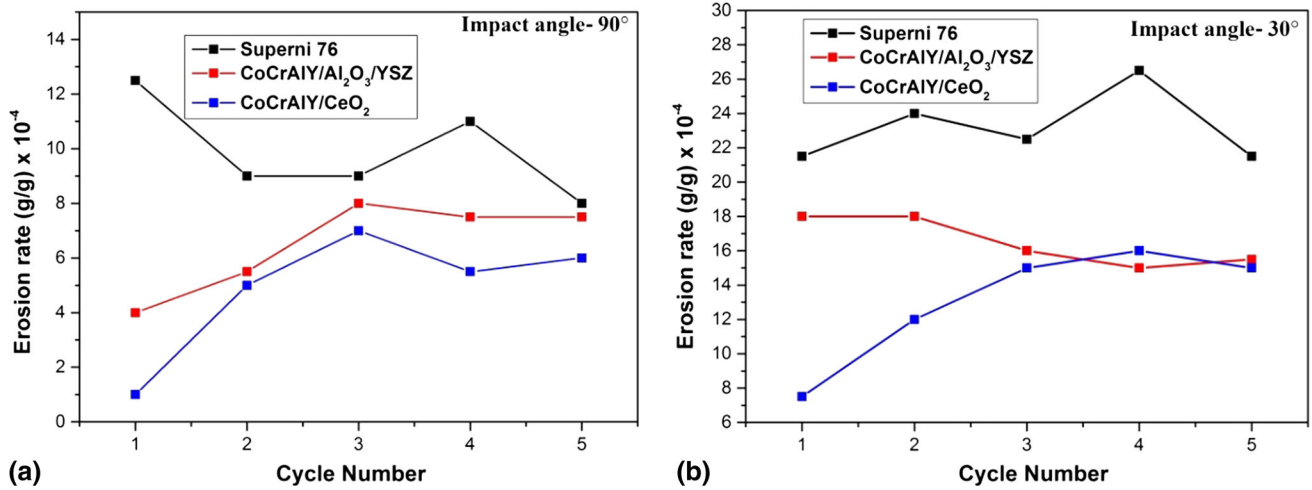
Fig. 9 Variations in erosion rate of uncoated, CoCrAlY/Al$_2$O$_3$/YSZ and CoCrAlY/CeO$_2$ coatings at 90° (a) and 30° (b) impact angles
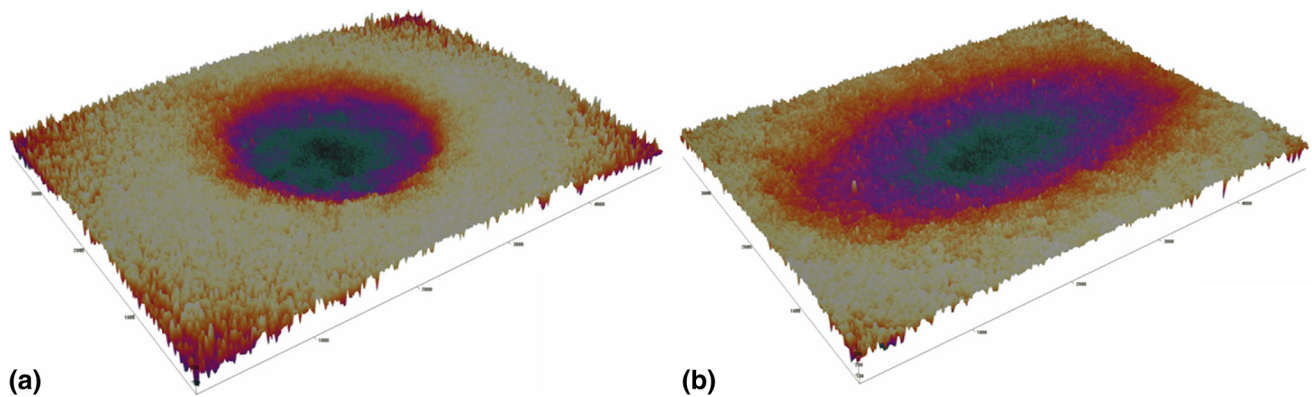

Fig. 10 3D profile of erosion scar at impact angle of 90° (a) and 30° (b)

occurs is modified by the protective oxide scale formed on the surface of coating. Coatings exhibit steady-state erosion with subsequent erosion cycles. The erosion at 30° is higher as compared 90° impact angle, which represents the ductile type of erosion behavior of the coating (Ref 14, 29, 30). Sunderarajan and Roy (Ref 30) reported that the dependence of erosion rate on impact angle is largely determined by the nature of target material. Ductile materials (like metals and alloys) exhibit a maximum erosion rate at intermediate impact angles (e.g., 15°, 30°). In contrast, the maximum erosion rate of a brittle material (like glass) is usually obtained at normal impact angle, i.e., at 90°.

Volumetric material losses from the eroded region are also determined through three-dimensional profile patterns generated using non-contact optical profilometer. All the measurements were taken on effective magnification of 5× with field view of 4.98 × 3.74 mm, so that the area of erosion scar is always within the analyzed area (field of view). Volume of eroded and uneroded regions is measured by locating deepest and highest step points within the scanning area. The erosion volume loss is calculated by taking the difference of volume of eroded region (V_2) and uneroded region (V_1). The difference between original and eroded surfaces at the deepest point was measured and designated as the erosion depth (Ref 22-24).

Figure 10 shows 3D profile of eroded scar region at impact angles of 90° and 30°, respectively. The erosion depth measured for both the coatings was observed to be within the range of 150 μm (Fig. 11). In case of CoCrAlY/Al$_2$O$_3$/YSZ coating, the erosion depth profile was 125 ± 5 μm at 90° impact angle and 73 ± 5 μm at 30° impact angle, whereas for CoCrAlY/CeO$_2$ coating the corresponding values were 104 ± 5 and 72 ± 5 μm. It is evident that both the coatings have sustained the erodent impact at both impact angles without allowing the erodent to penetrate into the bond coat at operating conditions of 600 °C. It was also observed that volumetric loss is more in case of 30° impact angle and erosion depth is more at 90° impact angle. This may be mainly because of the ductile nature of coating matrix and also due to large surface area covered by erodent particle during 30° impact angle. Volumetric erosion of coatings and substrate with different impact angles of 90° and 30° is represented using bar chart in Fig. 12. The CoCrAlY/Al$_2$O$_3$/YSZ coating shows volume loss of 2.5 and 3.3 mm^3 at 90° and 30° impact angles, respectively. The corresponding values in case of CoCrAlY/CeO$_2$ coating are 1.9 and 2.2 mm^3, implying that the volume loss incase of CoCrAlY/Al$_2$O$_3$/YSZ is 25% higher at 90° and 33% higher at 30°. In general, brittle material undergoes rapid erosion at higher angle than at lower angle of impact, and ductile material
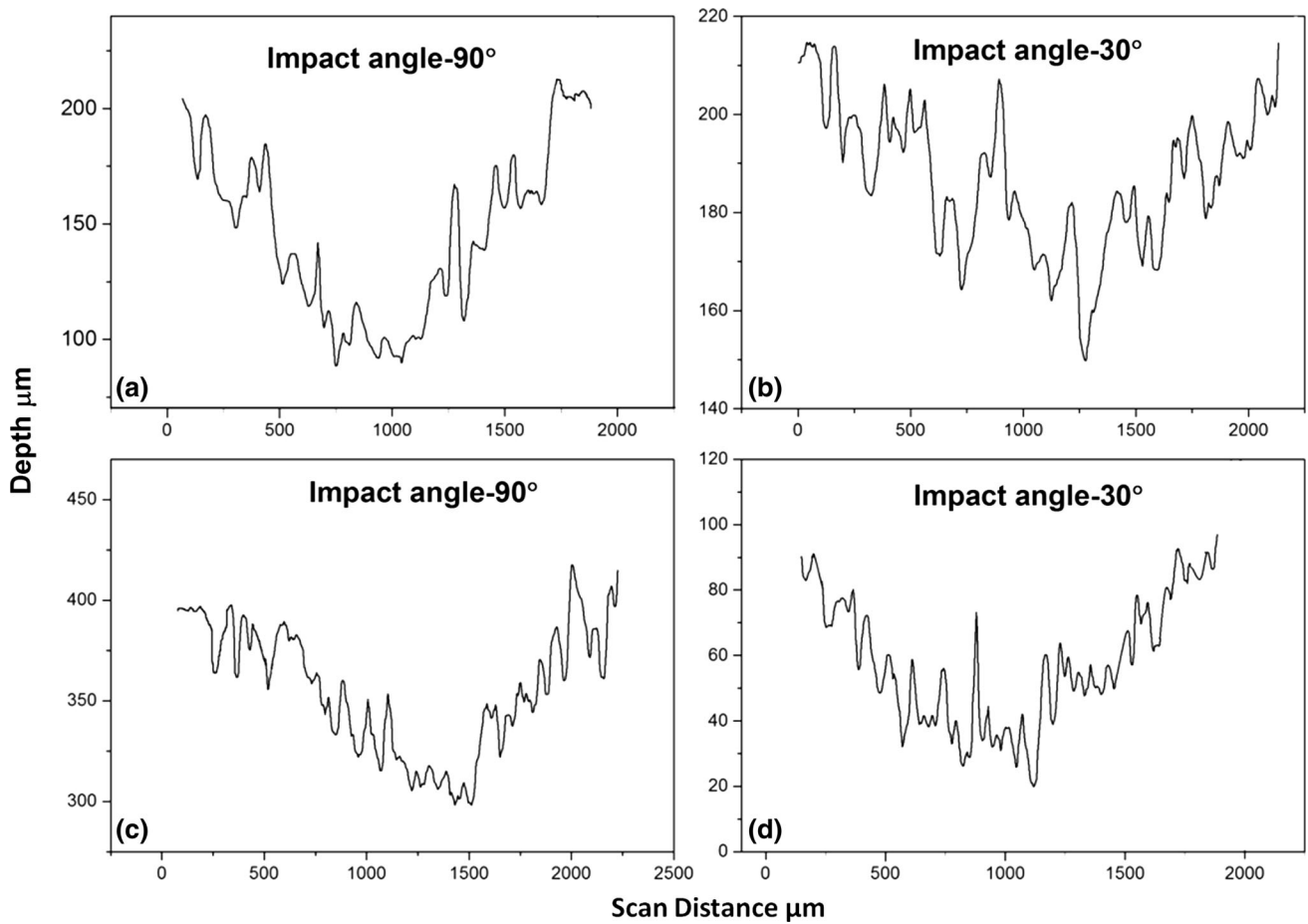
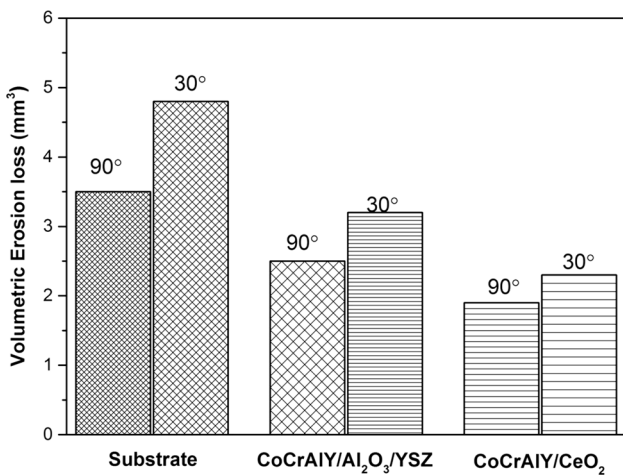**Fig. 11** Erosion depth profile of CoCrAlY/Al$_2$O$_3$/YSZ (a, b) and CoCrAlY/CeO$_2$ (c, d) coating

Fig. 12 Bar chart illustrating volumetric erosion loss at 90° and 30° impact angles

shows rapid erosion at lower angle than at higher angle of impact (Ref 14, 29, 30).

The protective behavior of the coating is related to the formation of surface oxides at operating temperature of 600 °C. Al, Cr, Co and Ce oxides on the surface act as barrier to the erodent impact and protect the coating. These surface oxides will erode with subsequent erosion cycles, and further coating will counter the erodent impact.

3.5 Erosion Mechanism

Surface morphology of erosion damage of CoCrAlY/Al$_2$O$_3$/YSZ and CoCrAlY/CeO$_2$ coating at 30° and 90° impact angles is shown in Fig. 13 and 14. At 90° impact angle, (Fig. 13a, 14a) erodent particle impinges normally on the surface. The continuous impact produces indents, resulting in raised lips at the periphery of indentation. The raised lips are formed due to plastic deformation under high strain rate. The deformed material is further removed from the surface in the form of platelets, pointing the ductile behavior of coating material at elevated temperature neglecting unusual oxide cracks. The shielding effect of reinforcement (alumina and ceria) reduces due to continuous impact of erodent, which weakens the boundary of splats, resulting in hard-phase detachment leaving behind craters (Ref 22). The craters are clearly visible in Fig. 13(a) and 14(a).

The EDS analysis of the fragments detached from the surface showed the composition rich in cobalt oxide. The fragment of CoO referred as region 1 in Fig. 13(a) is bigger in size than the platelets detached from the deformed raised lips. This may be attributed to higher oxidation rate at 600 °C in the initial cycles, thus forming protective oxide scales, which are responsible for steady-state erosion during subsequent erosion cycles. In case of CoCrAlY/CeO$_2$ coating, the oxides of Al and
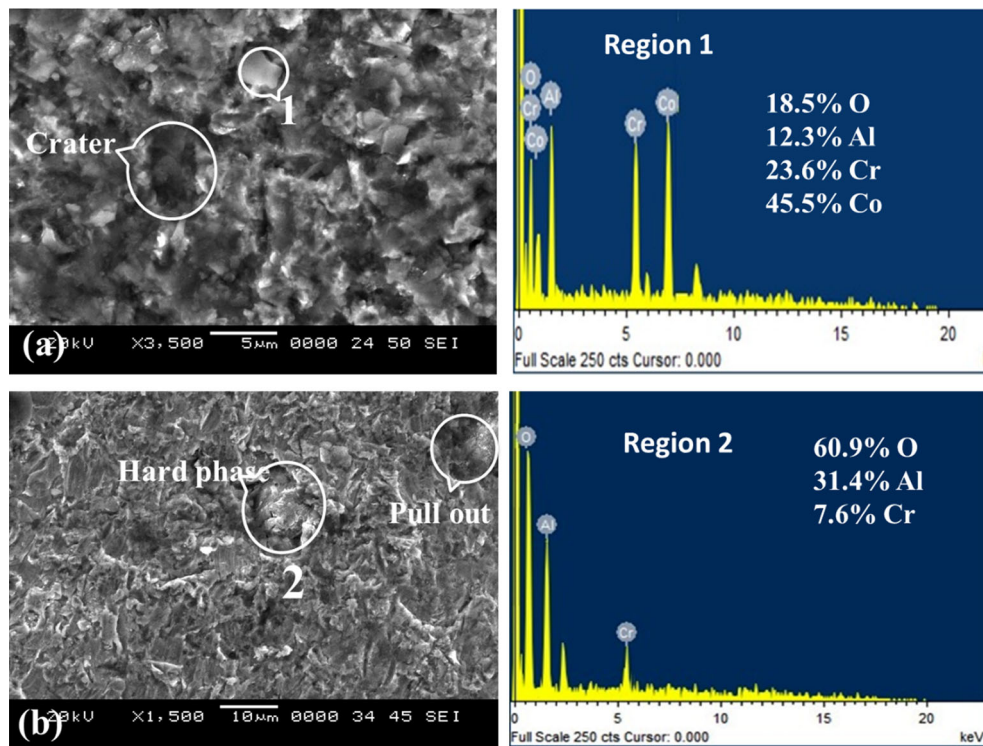
Fig. 13 Surface morphology and EDS analysis of CoCrAlY/Al$_2$O$_3$/YSZ coating showing eroded region with an impact angles of (a) 90° and (b) 30°, respectively
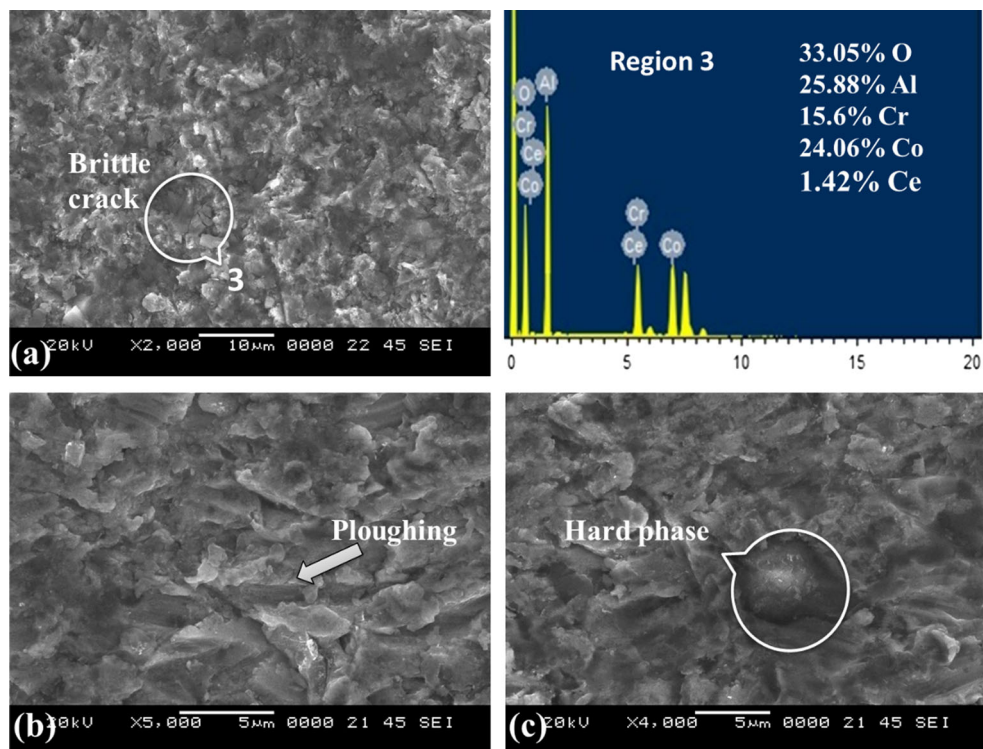

Fig. 14 Surface morphology and EDS analysis of CoCrAlY/CeO$_2$ coating showing eroded region with an impact angle of (a) 90° and (b, c) 30°, respectively

Co are evident at the brittle crack regions and are identified by EDS analysis referred as region 3 in Fig. 14(a). The presence of metal oxides also implies the occurrence of oxidation-modified erosion in CoCrAlY/CeO$_2$ coating.

At 30° impact angle (Fig. 13b, 14b) with erodent particle impinging at higher tangential force, severe plowing up marks are predominant on the eroded surface of both the coatings. Plowing, microcutting and craters are observed on the eroded surface confirming the ductile nature of coating and the material removal to be in the form of platelets. The angular erodent of higher particle size forms large groves on the surface by plowing mechanism. Plowing occurs mostly in the softer Co-based matrix region, and microcutting is due to the impact of tiny angular erodent particle.

Al$_2$O$_3$ hard phase surrounded by Co-based matrix restricts the material removal by taking impact load of the erodent. At 30° impact angle, the removal of material around Al$_2$O$_3$ particle (Fig. 13b) is due to repeated encounter of erodent that weakens the splat boundary resulting in hard-phase pull out. This accounts for the higher material loss at lower impact angle. The exposed hard-phase Al$_2$O$_3$ is identified by EDS analysis and represented as region 2 (Fig. 13b). Similar observations are conducted in CoCrAlY/CeO$_2$ coating where CeO$_2$ hard-phase pull out results in higher material loss at 30° impact angle of erodent. Few irregular craters are observed in CoCrAlY/CeO$_2$ coating, which may be due to smaller particle size and dense structure of CeO$_2$. From the above discussion, it can be inferred that both coatings show similar type of erosion mechanism.

The erosion volume loss and deformation are more in CoCrAlY/Al$_2$O$_3$/YSZ coating as compared to that of CoCrAlY/CeO$_2$ coating. This is because of erosion (deformation) response for crystalline and amorphous materials. It is observed that more amorphization is experienced in CoCrAlY/Al$_2$O$_3$/YSZ coating (Fig. 3). Greer (Ref 31) has also reported that amorphous material is more prone to shear band formation. The high strain evolved during erosion process favors the formation of shear band. In case of CoCrAlY/CeO$_2$ coating, CeO$_2$ acts as surface active element with other melted particles, which significantly reduces the surface tension and minimizes the unification of similar melted particles during spraying process by dispersing along the splat boundaries of coating material (Ref 13). This results in excellent wettability of CeO$_2$ which in turn increases the bonding between the splats of other coating elements, resulting in better erosion performance of CoCrAlY/CeO$_2$ coating.

4. Conclusions

1. Plasma spraying has been successfully used to obtain dense coating with thickness of 300 μm, and CoCrAlY/CeO$_2$ coating showed better coating properties.
2. The surface active nature of CeO$_2$ is the prime factor due to which unification of similar melted particles during spraying process is minimized and particles get dispersed along the splat boundaries of coating material. Thus, Co-CrAlY/CeO$_2$ coating showed better resistance to volumetric erosion at both 90° and 30° impact angle than CoCrAlY/Al$_2$O$_3$/YSZ coating.
3. Observations of plowing, microcutting, and hard-phase pullout features on the eroded surface of the coating at lower impact angle are the indications of ductile type of fracture.

4. The erosion response of coatings at high temperature is influenced by oxidation of active elements which culminate into oxidation-modified erosion behavior.

References

1. E. Bousser, L. Martinu, and J.E. Klemberg-Sapieha, Solid Particle Erosion Mechanisms of Protective Coatings for Aerospace Applications, *Surf. Coat. Technol.*, 2014, **257**, p 165–181
2. W. James and S. Rajagopalan, Gas turbines operating conditions, components and material requirements, *Structural Alloys for Power Plants. Woodhead Publishing Series in Energy*, A. Shirzadi and S. Jackson, Ed., Woodhead Publishing, Cambridge, 2014, p 3–21
3. W.T. Becker and R.J. Shipley, *Failure Analysis and Prevention, ASM Metals Handbook*, Vol 11, ASM Publication, Metals Park, 2002, p 1533
4. Y. Wang and W. Chen, Effect of Ceria on the Erosion Resistance of HVOF Thermal Sprayed NiAl Intermetallic Coatings, *J. Mater. Sci. Lett.*, 2003, **22**(11), p 845–848
5. B.S. Sidhu and S. Prakash, Performance of NiCrAlY, Ni–Cr, Stellite-6 and Ni$_3$Al Coatings in Na$_2$SO$_4$–60%V$_2$O$_5$ Environment at 900 °C Under Cyclic Conditions, *Surf. Coat. Technol.*, 2006, **201**(3), p 1643–1654
6. D. Seo, K. Ogawa, Y. Suzuki, K. Ichimura, T. Shoji, and S. Murata, Comparative Study on Oxidation Behaviour of Selected MCrAlY Coatings by Elemental Concentration Profile Analysis, *Appl. Surf. Sci.*, 2008, **255**(5), p 2581–2590
7. S. Sharma, Erosive Wear Study of Rare Earth-Modified HVOF-Sprayed Coatings Using Design of Experiment, *J. Therm. Spray Technol.*, 2012, **21**(1), p 49–62
8. N. Krishnamurthy, M.S. Murali, B. Venkataraman, and P.G. Mukunda, Characterization and Solid Particle Erosion Behavior of Plasma Sprayed Alumina and Calcia-Stabilized Zirconia Coatings on Al-6061 Substrate, *Wear*, 2012, **274**, p 15–27
9. Z. Yin, S. Tao, X. Zhou, and C. Ding, Tribological Properties of Plasma Sprayed Al/Al$_2$O$_3$ Composite Coatings, *Wear*, 2007, **263**(7), p 1430–1437
10. N. Ramanujam and T. Nakamura, Erosion Mechanisms of Thermally Sprayed Coatings with Multiple Phases, *Surf. Coat. Technol.*, 2009, **204**(1), p 42–53
11. H.J. Kim, S.Y. Hwang, C.H. Lee, and P. Juvanon, Assessment of Wear Performance of Flame Sprayed and Fused Ni-Based Coatings, *Surf. Coat. Technol.*, 2003, **172**(2), p 262–269
12. A. Mateen, G.C. Saha, T.I. Khan, and F.A. Khalid, Tribological Behaviour of HVOF Sprayed Near-Nanostructured and Microstructured WC-17 wt.% Co Coatings, *Surf. Coat. Technol.*, 2011, **206**(6), p 1077–1084
13. L. He, Y. Tan, H. Tan, Y. Tu, and Z. Zhang, Microstructure and Tribological Properties of WC-CeO$_2$/Ni-base Alloy Composite Coatings, *Rare Metal Mater. Eng.*, 2014, **43**(4), p 823–829
14. A.S. Praveen, J. Sarangan, S. Suresh, and J.S. Subramanian, Erosion Wear Behaviour of Plasma Sprayed NiCrSiB/Al$_2$O$_3$ Composite Coating, *Int. J. Refract. Met. Hard Mater.*, 2015, **52**, p 209–218
15. D. Zhao, F. Luo, W. Zhou, and D. Zhu, Effect of Critical Plasma Spray Parameter on Complex Permittivity and Microstructure by Plasma Spraying Cr/Al$_2$O$_3$ Coatings, *Appl. Surf. Sci.*, 2013, **264**, p 545–551
16. G. Shanmugavelayutham, S. Yano, and A. Kobayashi, Microstructural Characterization and Properties of ZrO$_2$/Al$_2$O$_3$ Thermal Barrier Coatings by Gas Tunnel-Type Plasma Spraying, *Vacuum*, 2006, **80**(11), p 1336–1340
17. N. Jegadeeswaran, M.R. Ramesh, and K.U. Bhat, Hot Corrosion Studies on As-Received and HVOF Sprayed Al$_2$O$_3$ + CoCrAlTaY on Ti-31 Alloy in Salt Environment, *Procedia Eng.*, 2013, **64**, p 1013–1019
18. G. Bolelli, A. Candeli, L. Lusvarghi, A. Ravaux, K. Cazes, A. Denoirjean, and L. Bianchi, Tribology of NiCrAlY + Al$_2$O$_3$ Composite Coatings by Plasma Spraying with Hybrid Feeding of Dry Powder + Suspension, *Wear*, 2015, **344**, p 69
19. N.R. Muktinutalapati, *Materials for Gas Turbines—An Overview*, INTECH Open Access Publisher, Rijeka, 2011

20. B. Movahedi, Fracture Toughness and Wear Behavior of NiAl-Based Nanocomposite HVOF Coatings, *Surf. Coat. Technol.*, 2013, **235**, p 212–219

21. A. Macwan, M. Marr, O. Kesler, and D.L. Chen, Microstructure, Hardness, and Fracture Toughness of Suspension Plasma Sprayed Yttria-Stabilized Zirconia Electrolytes on Stainless Steel Substrates, *Thin Solid Films*, 2015, **584**, p 23–28

22. M.R. Ramesh, S. Prakash, S.K. Nath, P.K. Sapra, and B. Venkataraman, Solid Particle Erosion of HVOF Sprayed WC-Co/NiCrFeSiB Coatings, *Wear*, 2010, **269**(3), p 197–205

23. M. Ivosevic, R. Knight, S.R. Kalidindi, G.R. Palmese, and J.K. Sutter, Solid Particle Erosion Resistance of Thermally Sprayed Functionally Graded Coatings for Polymer Matrix Composites, *Surf. Coat. Technol.*, 2006, **200**(16), p 5145–5151

24. P. Wiecinski, J. Smolik, H. Garbacz, and K.J. Kurzydlowski, Erosion Resistance of the Nanostructured Cr/CrN Multilayer Coatings on Ti6Al4V Alloy, *Vacuum*, 2014, **107**, p 277–283

25. M.P. Planche, H. Liao, B. Normand, and C. Coddet, Relationships Between NiCrBSi Particle Characteristics and Corresponding Coating Properties Using Different Thermal Spraying Processes, *Surf. Coat. Technol.*, 2005, **200**(7), p 2465–2473

26. T. Sundararajan, S. Kuroda, and F. Abe, Steam Oxidation Studies on 50Ni-50Cr HVOF Coatings on 9Cr-1Mo Steel: Change in Structure and Morphology Across the Coating/Substrate Interface, *Mater. Trans.*, 2004, **45**, p 1299–1305

27. T. Irisawa and H. Matsumoto, Thermal Shock Resistance and Adhesion Strength of Plasma-Sprayed Alumina Coating on Cast Iron, *Thin Solid Films*, 2006, **509**(1), p 141–144

28. S.A. Sadeghi-Fadaki, K. Zangeneh-Madar, and Z. Valefi, The Adhesion Strength and Indentation Toughness of Plasma-Sprayed Yttria Stabilized Zirconia Coatings, *Surf. Coat. Technol.*, 2010, **204**(14), p 2136–2141

29. Y. Wang, Y. Yang, and M.F. Yan, Microstructures, Hardness and Erosion Behaviour of Thermal Sprayed and Heat Treated NiAl Coatings with Different Ceria, *Wear*, 2007, **263**(1), p 371–378

30. G. Sundararajan and M. Roy, Solid Particle Erosion Behaviour of Metallic Materials at Room and Elevated Temperatures, *Tribol. Int.*, 1997, **30**(5), p 339–359

31. A.L. Greer, K.L. Rutherford, and I.M. Hutchings, Wear Resistance of Amorphous Alloys and Related Materials, *Int. Mater. Rev.*, 2002, **47**(2), p 87–112